



Plasmon echoes and polarization dynamics in Young's double-slit setup with pulsed light

Aleksi Leinonen ^{1,*} Henri Pesonen,^{1,2} Taco D. Visser ^{3,4,5} Jari Turunen,¹ and Ari T. Friberg¹

¹*Center for Photonics Sciences, University of Eastern Finland, P.O. Box 111, FI-80101 Joensuu, Finland*

²*Dispelix Oy, Yliopistokatu 7, FI-80130 Joensuu, Finland*

³*Department of Physics and Astronomy, Vrije Universiteit, Amsterdam 1081 HV, Netherlands*

⁴*The Institute of Optics, University of Rochester, Rochester, New York 14627, USA*

⁵*School of Physics and Electronics, Shandong Normal University, Jinan 250358, China*



(Received 29 March 2022; revised 13 October 2022; accepted 12 December 2022; published 27 December 2022)

We consider two closely spaced slits of subwavelength width, pierced in a metal screen, that are illuminated by short, arbitrarily polarized, plane-wave pulses. The p -polarized component generates plasmonic pulses propagating on the metal surface between the slits. In addition to the primary transmitted pulses, scattering of the plasmonic pulses by the opposite slit is found to produce secondary (echo) radiation pulses, which causes splitting, shaping, and time-dependent polarization modulation of the radiated pulses in the far field. We study these effects in the linear regime. A previously explored phenomenological model is extended to the time domain and is validated by rigorous numerical calculations. Our analytical and numerical results have implications for the transmission of pulsed light through arrangements of nanoscale apertures with plasmonic coupling.

DOI: [10.1103/PhysRevA.106.063519](https://doi.org/10.1103/PhysRevA.106.063519)

I. INTRODUCTION

Surface plasmon polariton (SPP) mediated effects in nanoapertures are a central part of nanophotonics that have numerous applications [1–5]. These effects include extraordinary optical transmission (EOT) [6], modulation of coherence and polarization [7–10], and directional excitation of SPPs [11–13]. Thus far, these effects have been studied for only continuous-wave quasimonochromatic illumination. In this work we introduce pulsed illumination for the double-slit setup. We restrict ourselves to the linear regime.

In a previous study [10] a phenomenological model for plasmon-modulated transmission through a double-slit setup was analyzed in detail. The model describes the optical transmission at each slit (for quasimonochromatic fields) as consisting of two contributions. The main one is due to direct transmission of the incident field. The other one is due to SPPs, generated at each slit, that travel on the metal film towards the adjacent slit, where they are partly scattered into a freely propagating field again [14–17]. The transmission is thus governed by the interference of these two fields, which in the general form for either one of the two apertures is

$$\mathbf{E} = \begin{bmatrix} E_x \\ E_y \end{bmatrix} = \begin{bmatrix} (\alpha + \gamma K)E_p \\ \beta E_s \end{bmatrix}. \quad (1)$$

In these expressions α and β are the transmission coefficients for p (TM) and s (TE) polarization, respectively. The factor γ describes the amplitude of the SPP contribution, and $K = \exp(ik_{\text{sp}}a)$ is the complex plasmon propagation factor over a distance a , with k_{sp} being the SPP wave number. To determine

the values of the three unknown parameters a rigorous numerical study was presented in [10]. The model was validated in the sense that for a given configuration (i.e., choice of metal and film thickness) the parameters remain essentially constant over a range of slit widths and separations. This means that the model not only successfully describes the mechanism behind EOT and coherence modification, as shown in [6–8], but can also be used to quickly optimize designs of systems with nanoapertures without having to resort to time-consuming rigorous analysis whenever a parameter is adjusted.

The assumption of the incident field being quasimonochromatic means that in the model the three parameters (α , β , and γ) are constants and thereby the model, in its original form, cannot be used in the context of pulsed fields. In this paper we extend the model to cover pulsed illumination by allowing the coefficients to be dispersive. We show that this leads to several new physical phenomena, including plasmons echoes and polarization-dependent pulse shaping.

The organization of this paper is as follows. In Sec. II the setup geometry and illumination are described. In Sec. III we present rigorous numerical examples of secondary “echo” pulses that are the result of SPPs. Next, in Sec. IV, a phenomenological model [6,7,10] for the double-slit configuration is extended to pulsed incident fields with any state of polarization. In Secs. V–VII we apply the analytical model to analyze SPP-induced pulse shaping and polarization modulation in the far zone and verify the results by rigorous numerical calculations.

II. SETUP AND ILLUMINATION

Figure 1 illustrates a two-slit system, where the sub-wavelength slits of width w are illuminated from below at normal incidence by Gaussian plane-wave pulses of length

*aleksi.leinonen@uef.fi

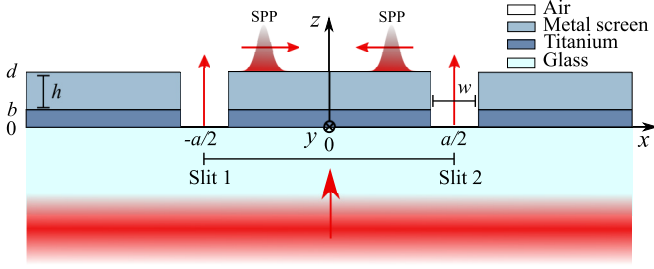


FIG. 1. Schematic of the two-slit system with pulsed illumination. The parameters are fixed as $w = 200$ nm, $h = 200$ nm, and $b = 20$ nm.

T and a time-independent polarization state. We remove the fast-oscillating carrier wave of (angular) frequency ω_0 by writing the temporal field at $z = 0$ in envelope form $\mathbf{E}(t) = \mathbf{a}(t) \exp(-i\omega_0 t)$, where

$$\mathbf{a}(t) = \begin{bmatrix} a_x(t) \\ a_y(t) \end{bmatrix} = E_0 \exp\left(-\frac{t^2}{T^2}\right) \begin{bmatrix} E_p \\ E_s \end{bmatrix}. \quad (2)$$

The (constant) p - and s -polarized components E_p and E_s , normalized such that $|E_p|^2 + |E_s|^2 = 1$, specify the incident state of polarization. The spectral representation of the incident field is

$$\mathbf{E}(\omega) = \begin{bmatrix} E_x(\omega) \\ E_y(\omega) \end{bmatrix} = \frac{E_0}{\sqrt{\pi}\Omega} \exp\left(-\frac{\tilde{\omega}^2}{\Omega^2}\right) \begin{bmatrix} E_p \\ E_s \end{bmatrix}, \quad (3)$$

where $\tilde{\omega} = \omega - \omega_0$, $\Omega = 2/T$, and we assume that $\Omega \ll \omega_0$. In our examples the carrier frequency is set as $\omega_0 = 2.38 \times 10^{15}$ rad/s, corresponding to the central wavelength $\lambda_0 = 792$ nm of a Ti:sapphire laser.

The incident field excites SPP pulses at both slits on the top side of the sample. Outwardly propagating SPP pulses are gradually attenuated due to Ohmic losses. However, SPPs generated at one slit that travel to the other slit can be scattered there into a freely propagating field in the $z > d$ half-space and thus produce what we call a ‘‘plasmon echo.’’ A thin layer of titanium prevents this process from happening on the lower side of the metal film.

The thickness h of the metal film is chosen to be sufficiently large to allow the use of the metal-air plasmon dispersion relation,

$$k_{\text{sp}}(\omega) = \frac{\omega}{c} \frac{n(\omega)}{\sqrt{1+n^2(\omega)}}, \quad (4)$$

where $n(\omega)$ is the complex refractive index of the metal and c is the speed of light in vacuum. For the metal we choose silver with $n(\omega_0) = 0.27 + i5.58$ at frequency $\omega = \omega_0$ [18], giving an SPP propagation length of $l_{\text{sp}} = 1/\text{Im}[k_{\text{sp}}(\omega_0)] \approx 77.6$ μm and an SPP wavelength of $\lambda_{\text{sp}} = 2\pi/\text{Re}[k_{\text{sp}}(\omega_0)] \approx 779$ nm. The other parameters are chosen as $w = 200$ nm, $h = 200$ nm, and $b = 20$ nm.

III. GENERATION OF THE PLASMON ECHO PULSE

The space-frequency field in the half-space $z \geq d$ is calculated rigorously by using the Fourier modal method (FMM) [10,19,20]. From this solution the temporal field $\mathbf{E}(\mathbf{r}, t) = [E_x(\mathbf{r}, t), E_y(\mathbf{r}, t), E_z(\mathbf{r}, t)]$ is obtained by Fourier integration

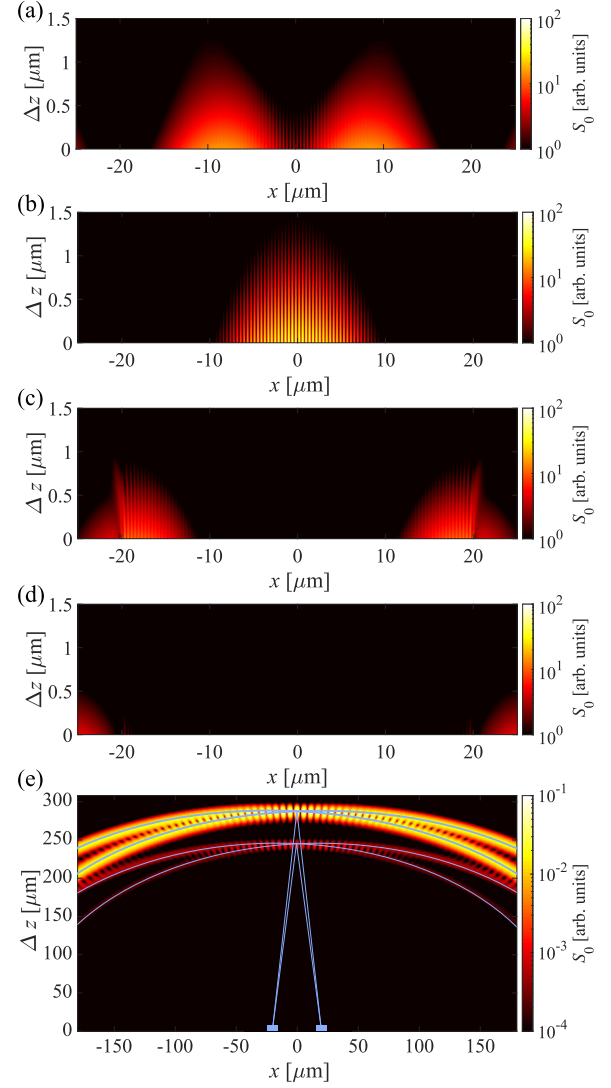


FIG. 2. Snapshots of the temporal intensity profiles $S_0(x, z, t)$ of fields propagating on and above the plane $z = d$, with $\Delta z = z - d$. The temporal profiles are obtained via FMM by Fourier integration over all spectral fields. Shown are near-field intensity profiles when (a) $t = 40.8$ fs, (b) $t = 67.0$ fs, (c) $t = 134.8$ fs, and (d) $t = 160.9$ fs. (e) Fresnel-domain temporal intensity profiles at $t = 1118.3$ fs. Time is measured from the arrival of the center of the incident pulse at the plane $z = 0$. Slits 1 and 2 are located at positions $x \approx -20$ μm and $x \approx +20$ μm , respectively, and are marked with blue rectangles. A video of near-field SPP propagation from $t = 1$ fs to $t = 167.6$ fs is provided in the Supplemental Material [22].

over all spectral components [21]. A detailed description of the calculations is presented in the Appendix. We first study p -polarized fields to focus solely on plasmonic effects. Figure 2 illustrates the results for a slit separation $a = 51.5\lambda_{\text{sp}}$ and pulse duration $T = 40$ fs. The temporal intensity profiles are given by

$$S_0(x, z, t) = |E_x(x, z, t)|^2 + |E_z(x, z, t)|^2, \quad (5)$$

where E_x and E_z represent the Cartesian components of the TM field ($E_s = E_y = 0$).

Figures 2(a)–2(d) and a video [22] illustrate plasmon excitation, propagation, and scattering into the near field. In Fig. 2(a) the pulses have emerged from the slits, and the primary radiation pulses that travel upwards are already outside the depicted $\Delta z = z - d$ range. Between the slits the counterpropagating SPPs form an interference pattern. In Fig. 2(b) the SPP pulses have traversed halfway through the distance a , while in Fig. 2(c) they have reached the other slit and are partially scattered, producing the echo radiation pulses. Figure 2(d) illustrates the part of the pulse that continues across the slit and is eventually absorbed by the metal. Based on our numerical calculations we estimate that about 1% of the total energy of the SPP pulse is reflected, 53% is transmitted, and 42% is converted into photons by the slit. The small portion of the SPP pulse reflected from the slit is visible as a slight interference around $x \approx \pm 20 \mu\text{m}$ in Fig. 2(d).

Figure 2(e) shows the space-time intensity distribution in the Fresnel region at $t = 1118.3$ fs, where the emanated primary radiation and the secondary echo pulses are visible simultaneously (notice the change of scale of both axes). The two radiation pulses interfere with each other, as do the two echo pulses. The circular arcs shown by the solid lines indicate the wave fronts of the pulses that originate from the pinholes.

The time delay Δt_d between the primary pulse and the echo is defined as the axial peak-to-peak time separation in the far zone. In this example we find $\Delta t_d = 142.1$ fs. The time separation could show angular dependence for off-axis far-zone directions. With longer incident pulses, the primary and echo pulses would partially overlap in time, leading to temporal pulse shaping rather than pulse splitting, as we will demonstrate in a later example. Additionally, higher-order echo pulses are generated by SPP pulses that undergo multiple reflections, but these are not visible due to their relatively low intensities.

IV. PHENOMENOLOGICAL TRANSMISSION MODEL FOR PULSES

We next proceed to formulate the phenomenological model for pulses in a plasmonic two-slit setup. For this purpose we evaluate rigorously the dispersion of the model coefficients using polarized monochromatic fields. For arbitrarily polarized quasimonochromatic fields the model was recently shown to be highly accurate with slit separations above $a \sim 10\lambda_{\text{sp}}$ [10]. As in the quasimonochromatic model in Eq. (1), the spectral field emerging from a single slit is

$$\mathbf{E}(\omega) = \begin{bmatrix} \alpha(\omega)E_p(\omega) + \gamma(\omega)K(\omega)E_p(\omega) \\ \beta(\omega)E_s(\omega) \end{bmatrix}, \quad (6)$$

where the frequency-dependent coefficients are determined for each frequency ω separately by using FMM.

The coefficient $\alpha(\omega)$ is obtained by considering a single slit illuminated by a p -polarized unit-amplitude field. It is taken as the field value at height $z = d$ in the center of the slit. The evanescent part of the field is filtered out, and only the propagating part remains. The coefficient $\beta(\omega)$ is determined similarly, but with a unit-amplitude s -polarized field as input.

The scattering plasmon coefficient $\gamma(\omega)$ is found by analyzing a unit-amplitude p -polarized illumination on a double-slit structure, in which slit 1 is open but the direct

transmission is blocked at slit 2. The two beams of complex amplitudes $\alpha(\omega)$ (slit 1) and $\gamma(\omega)K(\omega)$ (slit 2) then interfere in the far zone. The resulting normalized spectral intensity pattern and fringe visibility near the forward direction are of the form [10]

$$S'_0(\theta, \omega) = |\alpha(\omega)|^2 + |\gamma(\omega)|^2 \exp\{-2\text{Im}[k_{\text{sp}}(\omega)a]\} + 2|\alpha(\omega)||\gamma(\omega)| \exp\{-\text{Im}[k_{\text{sp}}(\omega)]a\} \times \cos\{\arg \gamma(\omega) - \arg \alpha(\omega) + \text{Re}[k_{\text{sp}}(\omega)]a - k_0(\omega)\theta a\}, \quad (7)$$

$$V(\omega) = \frac{2|\alpha(\omega)||\gamma(\omega)| \exp\{-\text{Im}[k_{\text{sp}}(\omega)]a\}}{|\alpha(\omega)|^2 + |\gamma(\omega)|^2 \exp\{-2\text{Im}[k_{\text{sp}}(\omega)]a\}}, \quad (8)$$

where Re and Im stand for the real and imaginary parts, respectively. It is seen that the phase of $\gamma(\omega)$ is obtained from the direction θ_0 of maximum $S'_0(\theta, \omega)$, which is attained when the argument of the cosine term in Eq. (7) is zero. The absolute value $|\gamma(\omega)|$ can be computed from $V(\omega)$ using Eq. (8) when $|\alpha(\omega)|$ is known. In the determination of $\gamma(\omega)$ the slit separation a was set near the plasmon propagation length l_{sp} to suppress the effects of SPPs reflected between the slits. We averaged $\gamma(\omega)$ using 20 different slit separations over $2\lambda_{\text{sp}}$ for better statistical accuracy. As a result, γ is independent of the SPP propagation distance a .

The dispersive behavior of the model coefficients for silver is illustrated in Fig. 3 over a wavelength range of 752–842 nm. We attribute the peaks in $|\gamma(\omega)|$ to minor numerical instabilities, further explained in the Appendix. From Fig. 3(a) we observe that the amplitudes of the coefficients vary fairly slowly. We have found that the ap-

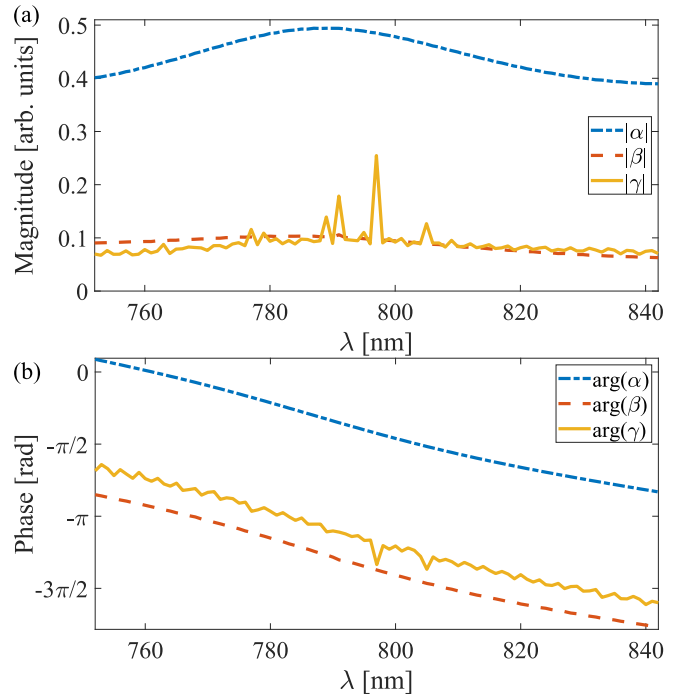


FIG. 3. Dispersion of the model coefficients α (blue dash-dotted line), β (red dashed line), and γ (yellow solid line) for silver: (a) magnitudes and (b) unwrapped phases.

TABLE I. Model coefficients $\zeta(\omega)$ for silver with center wavelength $\lambda_0 = 792$ nm. These values are for a slit with both a width and height of 200 nm. The rms errors are given for magnitude ϵ_{abs} and phase ϵ_{arg} , whereas the standard errors ϵ_c are given for the phase slopes.

$\zeta(\omega)$	$ \zeta(\omega_0) $	ϵ_{abs}	$\arg[\zeta(\omega_0)]$	ϵ_{arg}	C_ζ	ϵ_c
$\alpha(\omega)$	0.493	± 0.061	-1.144 rad	± 0.054	26.9	± 0.2
$\beta(\omega)$	0.101	± 0.020	2.168 rad	± 0.072	27.1	± 0.2
$\gamma(\omega)$	0.097	± 0.025	2.757 rad	± 0.094	27.7	± 0.3

proximation $|\zeta(\omega)| = |\zeta(\omega_0)|$, $\zeta(\omega) = \alpha(\omega)$, $\beta(\omega)$, $\gamma(\omega)$, is warranted since the bandwidth satisfies $\Omega \ll \omega_0$. The phases $\arg[\zeta(\omega)]$ in Fig. 3(b) are approximately linear, which allows us to write

$$\zeta(\omega) = \zeta(\omega_0) \exp(iC_\zeta \tilde{\omega}/\omega_0), \quad (9)$$

where $\tilde{\omega} = \omega - \omega_0$, as before, and C_ζ denotes the dispersive phase slope. The phase slopes are calculated from the FMM data set by linear least-squares estimation [23]. The coefficients, standard errors of the phase slopes ϵ_c , and the rms errors (magnitude ϵ_{abs} and phase ϵ_{arg}) are collected in Table I, corresponding to the geometry of Fig. 1. In particular, the phase slopes C_α and C_β are nearly identical, with values residing within the standard-error ranges of each other, even though the absolute values and phases of $\alpha(\omega_0)$ and $\beta(\omega_0)$ at the center wavelength of 792 nm are different. Further, the phase slope C_γ differs from the others and has a higher value. We note that $|\alpha(\omega_0)| \approx 5|\gamma(\omega_0)|$, indicating that the echo is weaker than the primary, directly transmitted pulse.

V. ANALYTICAL MODEL FOR FAR-FIELD RADIATION FOR PULSES

In order to utilize Eq. (9) in an analytical expression we first consider the spectral electric field in the paraxial region of the far zone, where the E_z component is approximately zero. The derivations are presented with the carrier frequency ω_0 exposed. The spatial frequencies of the field that contribute in the far zone are defined as $k_x = k_0(\omega/\omega_0) \sin \theta$, where $k_0 = \omega_0/c$ and θ is the diffraction angle as measured from the z direction. The field is expressed in the form (Eq. (A5) of [10])

$$\mathbf{E}(x, z, \omega) = \sqrt{2\pi k_0/\Delta z} \exp(-i\pi/4) \mathbf{E}(\theta, \omega), \quad (10)$$

where $\Delta z = z - d$. The far field $\mathbf{E}(\theta, \omega)$ in the near forward direction ($\theta \approx 0$) is directly related to the angular spectrum $\mathbf{A}(k_x, \omega)$ of the electric field as

$$\mathbf{E}(\theta, \omega) = \sqrt{\omega/\omega_0} \mathbf{A}(k_0\theta\omega/\omega_0, \omega) \exp\left(\frac{ik_0\Delta z\omega}{\omega_0}\right). \quad (11)$$

Here, the frequency-dependent components $A_x(k_x, \omega)$ and $A_y(k_x, \omega)$ follow from the phenomenological model when the two slits are taken as appropriate line sources [10]. The components assume the form

$$A_x(k_x, \omega) = E_x(\omega)[\alpha(\omega) + \gamma(\omega)K(\omega)] \cos\left(\frac{k_x a}{2}\right), \quad (12)$$

$$A_y(k_x, \omega) = E_y(\omega)\beta(\omega) \cos\left(\frac{k_x a}{2}\right), \quad (13)$$

where the $\cos(k_x a/2)$ factors follow from the symmetry of the two slits.

To isolate the carrier wave we express the electric field in the envelope form $\mathbf{E}(\theta, t_r) = \mathbf{a}(\theta, t_r) \exp(-i\omega_0 t_r)$, where $t_r = t - \Delta z/c$. The time-domain contribution $\mathbf{a}(\theta, t_r)$ is obtained by Fourier transforming Eq. (11) as

$$\mathbf{a}(\theta, t_r) = \int_0^\infty \sqrt{\omega/\omega_0} \mathbf{A}(k_0\theta\omega/\omega_0, \omega) \exp(-i\tilde{\omega} t_r) d\omega. \quad (14)$$

Since $\Omega \ll \omega_0$, we may approximate $\sqrt{\omega/\omega_0} \approx 1$ in Eq. (14) and replace the lower integration limit by $-\infty$. By the same argument we may ignore the dispersion of $n(\omega)$ in Eq. (4) and express the effective complex refractive index as

$$N = N_r + iN_i = \frac{n(\omega_0)}{\sqrt{1 + n^2(\omega_0)}}. \quad (15)$$

Using this notation, we can write the SPP's complex propagation factor as

$$K(\omega) = K(\omega_0) \exp[iN(a/c)\tilde{\omega}], \quad (16)$$

where

$$K(\omega_0) = \exp(-N_i\omega_0 a/c) \exp(iN_r\omega_0 a/c). \quad (17)$$

On inserting Eqs. (3), (9), (12), and (13) into Eq. (14) and integrating, we find analytical expressions for $a_x(\theta, t_r)$ and $a_y(\theta, t_r)$. If we set $\theta = 0$, the analytical expressions for the temporal-field components simplify to

$$\begin{aligned} a_x(0, t_r) = & E_0 E_p \alpha(\omega_0) \exp\left[-\frac{(t_r - C_\alpha/\omega_0)^2}{T^2}\right] \\ & + E_0 E_p \gamma(\omega_0) K(\omega_0) \\ & \times \exp\left[-\frac{(t_r - C_\gamma/\omega_0 - Na/c)^2}{T^2}\right] \end{aligned} \quad (18)$$

and

$$a_y(0, t_r) = E_0 E_s \beta(\omega_0) \exp\left[-\frac{(t_r - C_\beta/\omega_0)^2}{T^2}\right]. \quad (19)$$

In Eq. (18) the first and second terms correspond to the primary and echo pulses, respectively.

Using the relation $N = N_r + iN_i$ in the exponential term of the echo contribution in Eq. (18), we see that only the real part of N affects the temporal location of the echo pulse. As the plasmon speed on the interface is $v_{\text{sp}} = \omega_0/\text{Re}[k_{\text{sp}}(\omega_0)] = N_r/c$, the time delay caused by the SPP propagation between the slits is $\tau = N_r a/c$. Therefore, the time separation between the primary and echo pulses from Eq. (18) assumes the form

$$\Delta t_r = (C_\gamma - C_\alpha)/\omega_0 + \tau. \quad (20)$$

Since $C_\alpha \approx C_\beta$, the primary p and s pulses have a negligible time delay, according to dispersive response theory [24], whereas the difference between C_γ and C_α implies that the SPP-photon conversion process is dispersive and induces, in our case, an additional time delay of $\Delta t_c = (C_\gamma - C_\alpha)/\omega_0 \approx 0.3$ fs that is independent of the SPP propagation distance. Because the coefficient $\alpha(\omega)$ refers to a process that does not involve SPPs, whereas $\gamma(\omega)$ involves SPP conversions from light and to light, we interpret Δt_c as the time delay introduced by the SPP conversion process.

VI. PULSE SHAPING AND SPLITTING

If the time shift Δt_r is larger than T , as in Fig. 2, the primary and echo pulses are separated temporally in the far field, and in the phenomenological model their individual intensity profiles become Gaussian with pulse duration T . Figure 4(a) illustrates this splitting with the same parameters as in Fig. 2, i.e., $a = 51.5\lambda_{\text{sp}}$ and $T = 40$ fs. The solid green line represents the pulse shape given by Eq. (14), with $A_x(0, \omega)$ determined by FMM analysis, and the dashed blue line is the result given by the phenomenological model, Eq. (18), with parameters from Table 1. We see good agreement between the two approaches.

For longer pulses, with $T \sim \Delta t_r$, the primary and echo pulses interfere, and the shape of the combined pulse differs from the Gaussian form. In the region where the two pulses overlap, we generally see quasiperiodic changes of the intensity profile as a function of a , featuring alterations in the plasmon propagator $K(\omega)$. The factor $K(\omega)$ changes sign when a is altered by half a plasmon wavelength λ_{sp} , manifesting constructive or destructive interference. The pulse-shaping

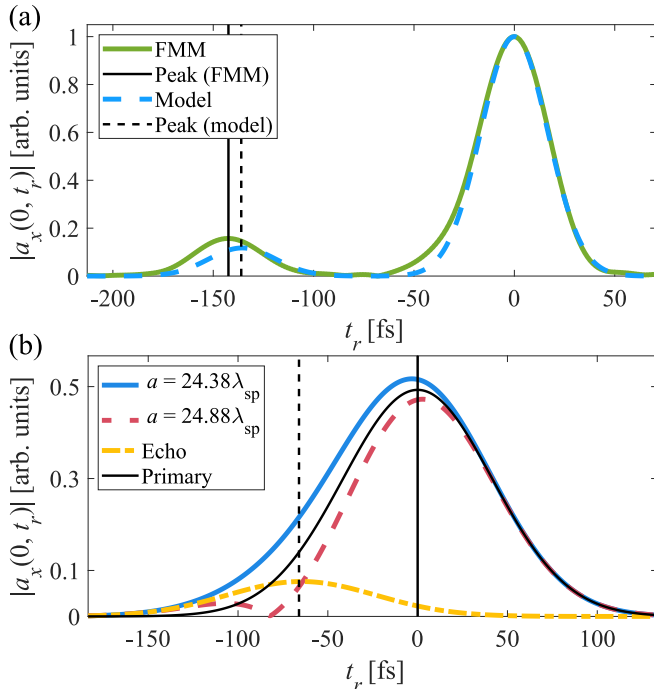


FIG. 4. (a) Pulse splitting in the far zone with slit separation $a = 51.5\lambda_{\text{sp}}$ for a p -polarized $T = 40$ fs pulse: distributions of $|a_x(0, t_r)|$ given by FMM analysis (solid green line) and the phenomenological model (dashed blue line). Both are normalized to their maximum values, and the maxima of the primary pulses are set to 1 for comparison. The two vertical lines indicate the moment when the echo pulse reaches its maximum, according to FMM and the model. (b) Pulse shaping by the plasmon echo for a p -polarized $T = 100$ fs pulse: distributions of $|a_x(0, t_r)|$ in the cases of constructive $a = 24.38\lambda_{\text{sp}}$ (solid blue line) and destructive $a = 24.88\lambda_{\text{sp}}$ (dashed red line) interference. The individual contributions of the primary [$\gamma(\omega_0) = 0$ in Eq. (18)] and echo pulses [$\alpha(\omega_0) = 0$ in Eq. (18)] are shown by the solid black and dash-dotted yellow lines, respectively. The vertical lines indicate the maxima of these contributions.

phenomena predicted by the phenomenological model are illustrated quantitatively in Fig. 4(b). Here we consider p -polarized $T = 100$ fs incident pulses for slit separations of $a = 24.38\lambda_{\text{sp}}$ (solid blue line) and $a = 24.88\lambda_{\text{sp}}$ (dashed red line). These correspond to the constructive and destructive interferences, respectively, between which plots for other (close) values of a are bounded. The shapes of the primary (solid black line) and echo (dash-dotted yellow line) pulses, given by the first and second terms in Eq. (18), are also shown for clarity. Inspection of Fig. 4(b) shows that wavelength-scale changes of a have (perhaps unexpectedly) a significant effect on the temporal shape of the total far-field pulse. With destructive interference the total pulse becomes $\sim 6.4\%$ narrower than the primary (and the incident) pulse, whereas with constructive interference it is widened by $\sim 8.3\%$.

VII. POLARIZATION DYNAMICS

Proceeding to consider polarization dynamics of pulses in the far zone, the polarization state of the incident field is determined by the polarization matrix [25]

$$\mathbf{J} = \begin{bmatrix} J_{pp} & J_{ps} \\ J_{sp} & J_{ss} \end{bmatrix} = \begin{bmatrix} \langle E_p^* E_p \rangle & \langle E_p^* E_s \rangle \\ \langle E_s^* E_p \rangle & \langle E_s^* E_s \rangle \end{bmatrix}, \quad (21)$$

where the asterisk and the brackets denote complex conjugation and ensemble averaging, respectively, and normalize it such that $\text{tr } \mathbf{J} = J_{pp} + J_{ss} = 1$. We represent the incident field as a sum of unpolarized and fully polarized parts, where the latter is linearly polarized at an angle ϕ measured from the x axis. The elements of \mathbf{J} are expressed as [10]

$$J_{pp} = \frac{1}{2}(1 - P_i) + P_i \cos^2 \phi, \quad (22a)$$

$$J_{ps} = J_{sp} = P_i \sin \phi \cos \phi, \quad (22b)$$

$$J_{ss} = \frac{1}{2}(1 - P_i) + P_i \sin^2 \phi, \quad (22c)$$

where P_i denotes the degree of polarization of the incident field [25]. The far-field temporal polarization matrix in the paraxial direction θ is defined as

$$\begin{aligned} \Phi(\theta, t_r) &= \mathbf{a}^*(\theta, t_r) \mathbf{J} \mathbf{a}^T(\theta, t_r) = \begin{bmatrix} \Phi_{xx}(\theta, t_r) & \Phi_{xy}(\theta, t_r) \\ \Phi_{yx}(\theta, t_r) & \Phi_{yy}(\theta, t_r) \end{bmatrix} \\ &= \begin{bmatrix} J_{pp} a_x^*(\theta, t_r) a_x(\theta, t_r) & J_{ps} a_x^*(\theta, t_r) a_y(\theta, t_r) \\ J_{sp} a_y^*(\theta, t_r) a_x(\theta, t_r) & J_{ss} a_y^*(\theta, t_r) a_y(\theta, t_r) \end{bmatrix}, \end{aligned} \quad (23)$$

where the superscript T denotes the transpose. The temporal polarization properties are characterized by the time-dependent Stokes parameters

$$S_0(\theta, t_r) = \Phi_{xx}(\theta, t_r) + \Phi_{yy}(\theta, t_r), \quad (24a)$$

$$S_1(\theta, t_r) = \Phi_{xx}(\theta, t_r) - \Phi_{yy}(\theta, t_r), \quad (24b)$$

$$S_2(\theta, t_r) = \Phi_{xy}(\theta, t_r) + \Phi_{yx}(\theta, t_r), \quad (24c)$$

$$S_3(\theta, t_r) = i[\Phi_{yx}(\theta, t_r) - \Phi_{xy}(\theta, t_r)] \quad (24d)$$

and the time-dependent degree of polarization

$$P(\theta, t_r) = \sqrt{s_1^2(\theta, t_r) + s_2^2(\theta, t_r) + s_3^2(\theta, t_r)}, \quad (25)$$

where $s_n(\theta, t_r) = S_n(\theta, t_r)/S_0(\theta, t_r)$, $n = 1, 2, 3$, are the normalized Stokes parameters. In the following analysis we focus

on the on-axis polarization dynamics, i.e., $\theta = 0$, and suppress θ from the expressions.

Figure 5 illustrates the time-dependent polarization properties of the total field under conditions where the incident pulse is partially polarized and the echo pulse partially overlaps with both the primary p pulse and the s pulse. The center of the primary pulse is located at $t_r = 0$ fs. In Fig. 5(a) we take the same values of a and T as in Fig. 4(b) but consider the case $P_i = 0.92$, $\phi = 90^\circ$. We present both constructive ($a = 24.38\lambda_{\text{sp}}$) and destructive ($a = 24.88\lambda_{\text{sp}}$) echo interference, distinguished by the phase the propagating plasmon has acquired, as discussed in Sec. V. The predominantly s -polarized incident pulse was chosen such that the output pulses would be unpolarized without the echo contribution; that is, we would have $P(t_r) = 0$ when neglecting the echo. With the echo taken into account the degree of polarization $P(t_r)$ varies significantly over time due to the dynamics of $s_1(t_r)$, whereas the changes in the intensity are negligible. This behavior is caused by the mainly s -polarized nature of the incident pulse, where the only p -polarized contribution is induced from the tiny unpolarized part of the incident pulse. Since the echo is fully p polarized, the second and third Stokes parameters remain zero.

In Fig. 5(b) the parameters are chosen as $T = 100$ fs, $P_i = 0.8$, and $\phi = 80^\circ$, implying that all three normalized Stokes parameters vary with time. We set the echo at the tail of the primary pulse ($t_r = -52$ fs) to illustrate a case in which the handedness of the elliptical polarization state is switched by the echo pulse, achieved with slit separations $a = 19.09\lambda_{\text{sp}}$ and $a = 19.73\lambda_{\text{sp}}$, respectively. In this case the plasmon echo causes a gradual change in all three Stokes parameters with negligible modulation in the intensity due to the primary pulse being mainly s polarized. A slight deviation between the degrees of polarization is observed around $t_r \approx 80$ fs.

Next, in Fig. 5(c), a case of a substantially p -polarized incident pulse ($T = 100$ fs, $P_i = 0.70$, $\phi = 40^\circ$) is studied. The pulses emerging from the slits have a dominant p -polarized part, and no large changes take place in the degree of polarization. The Stokes parameters $s_1(t_r)$ and $s_2(t_r)$, however, undergo a rapid change near the tail of the primary pulse ($t_r = -80$ fs) for destructive interference ($a = 20.88\lambda_{\text{sp}}$), while the changes in polarization with constructive ($a = 20.38\lambda_{\text{sp}}$) interference are negligible. With mainly p -polarized light the changes in intensity become large in comparison to the s -polarized cases examined in Figs. 5(a) and 5(b). Similar behavior can be induced by allowing P_i to be small, since $|\alpha(\omega)| \geq 4|\beta(\omega)|$.

The results in Figs. 5(a)–5(c) indicate that for mainly s -polarized light the plasmonic effects mostly reside in the temporal polarization of the pulse, meaning that we can introduce gradual polarization dynamics with s -polarized pulses with little change in intensity. Conversely, use of p -polarized light induces high variation in the intensity, but the effects on polarization dynamics are small.

VIII. CONCLUSIONS

In summary, this analytical and numerical study extends the phenomenological model for a continuous-wave plasmon-

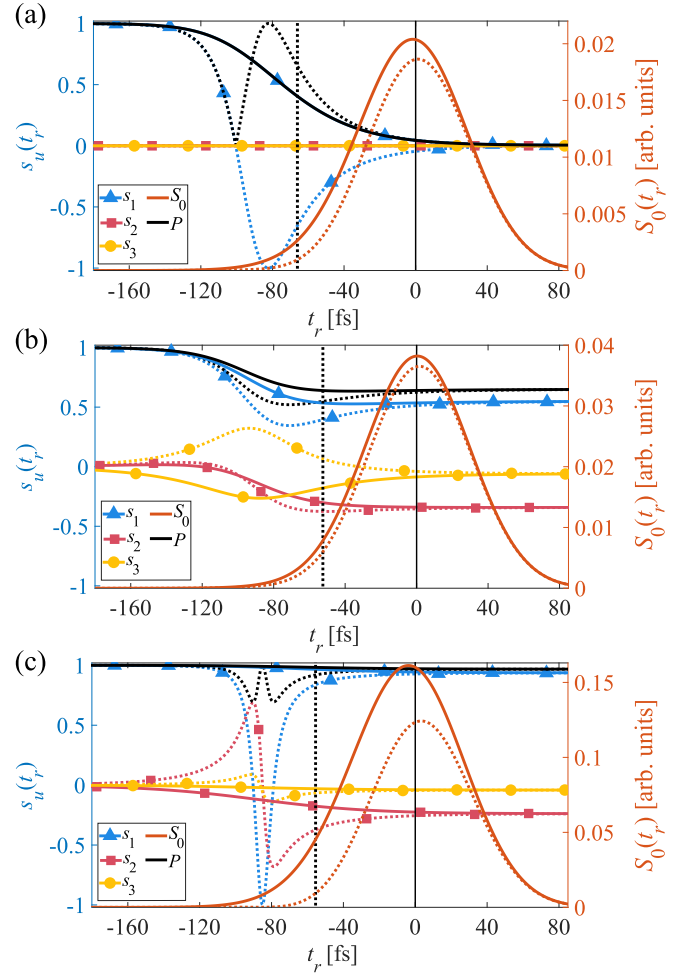


FIG. 5. Intensity $S_0(t_r)$, the normalized Stokes parameters $s_n(t_r)$, and the degree of polarization $P(t_r)$ for the analyzed cases. (a) $T = 100$ fs, $P_i = 0.92$, $\phi = 90^\circ$, with slit separations set to constructive $a = 24.38\lambda_{\text{sp}}$ (solid lines) and destructive $a = 24.88\lambda_{\text{sp}}$ (dotted lines) interference. (b) $T = 100$ fs, $P_i = 0.80$, $\phi = 80^\circ$ with slit separations of $a = 19.09\lambda_{\text{sp}}$ (solid lines) and $a = 19.73\lambda_{\text{sp}}$ (dashed lines). (c) $T = 100$ fs, $P_i = 0.70$, $\phi = 40^\circ$, with slit separations set to constructive $a = 20.38\lambda_{\text{sp}}$ (solid lines) and destructive $a = 20.88\lambda_{\text{sp}}$ (dotted lines) interference. In (a)–(c) the vertical lines show the centers of the primary (solid) and echo (dotted) p pulses.

assisted Young's experiment to pulsed light with an arbitrary state of polarization. The model was validated by comparison with rigorous diffraction analysis. We found that the excitation of SPPs and their subsequent conversion into light cause pulse splitting, pulse shaping, and a change in polarization over time. The precise form of these effects depends on whether the SPP echo overlaps with the primary pulse or not.

Notably, the significant effects related to constructive or destructive interference from the SPP pulse propagation should be taken into account in the design of metallic nanoscale apertures. Shaping effects could be enhanced by implementing dielectric ridges on the outer sides of the slits to scatter the remaining SPP energy and increase the intensity

of the echo pulse, but this would also change the shape of the far-field pattern. Dispersion of the metal film, as shown in Fig. 3(b), creates an SPP pulse with a delayed center frequency. In this study we restricted ourselves to linear effects, meaning that the effects we have described always occur. At high intensities one would also have to take nonlinear effects into account [26,27].

Light transmission through a set of nanoscale apertures involves a complex interplay between waveguide modes, surface plasmons, surface corrugations, and field singularities like vortices and saddle points. It is by a simple and clean setup like Young's double-slit experiment that the crucial role of SPPs can be disentangled from the other contributions [28]. Conversely, the significant effects of SPPs on the transmission of pulsed fields that we have presented here in a double-slit context are predicted to also occur in more complex arrangements of nanosized apertures in metal films.

ACKNOWLEDGMENTS

This research was funded by the Academy of Finland (Grants No. 333938 and No. 320166 PREIN). A.L. acknowledges funding from the Finnish Cultural Foundation. T.D.V. thanks the Joensuu University Foundation for support the Finnish Cultural Foundation.

APPENDIX: FOURIER MODAL METHOD AND CONVERGENCE OF THE CALCULATIONS

The Fourier modal method is a rigorous computational method based on calculating monochromatic fields in the frequency domain [19,20]. The FMM always assumes spatial periodicity, and to apply it in an aperiodic nanoslit configuration (such as ours) we are required to use either large computational periods or perfectly matched layers (PMLs). Our implementation of FMM is based on the S -matrix formulation [19] with gradually applied PMLs, where we have also employed a coordinate transform to the edges. The width of the PML zones for each edge was set as $20\ \mu\text{m}$, and the coordinate transform is applied $8\ \mu\text{m}$ from the edges of the period. These boundaries implemented on both sides of the computational area [see Fig. 6(a)] guarantee aperiodicity. An additional benefit of using PMLs is the reduced computational period, which reduces the truncation order required for the calculations to converge [20].

The convergence of the simulations is analyzed by defining the desired setup and calculating the efficiency of the first diffraction order as a function of the truncation order. Figure 6(b) shows the convergence in the system we used to compute the coefficients $[\alpha(\omega), \beta(\omega), \gamma(\omega)]$ presented in Fig. 3, where the computational period D is $170\ \mu\text{m}$. This period was chosen since we define the coefficient γ when the two slits are located one SPP decay length $l_{\text{sp}} = 1/\text{Im}[k_{\text{sp}}(\omega)]$ apart, which is approximately $101\ \mu\text{m}$ for the last wavelength (852 nm) of the calculated pulse (see Fig. 3). Here we have also fixed $w = 200\ \text{nm}$, $h = 200\ \text{nm}$, and $b = 20\ \text{nm}$. The refractive indices for silver and Ti are taken from [18]. From Fig. 6(b) we see that although the calculations are already converged for $o = 1500$, we opted to use 2500 as our trunca-

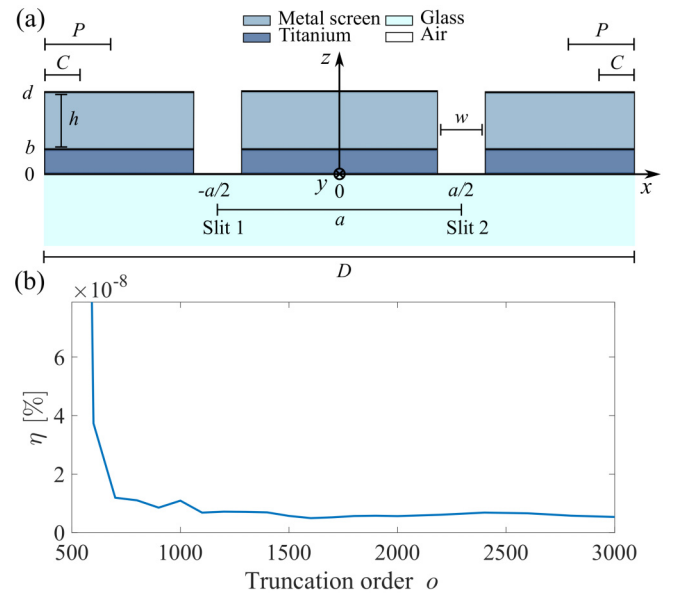


FIG. 6. (a) An illustration of the defined geometry, where D is the computational period, C is the coordinate transform zone, P is the PML zone, a is the slit separation, b is the thickness of Ti layer, h is the thickness of the metal screen, d is the thickness of the grating, w is the width of the slit, and x, y, z are the spatial axes. (b) Convergence of FMM calculations for determination of the coefficients. The convergence is checked from the diffraction efficiency η of the positive first transmitted diffraction order as a function of truncation order o .

tion order. In Table II we give the calculation periods and the truncation orders for all FMM simulations used in this study.

From the converged results we notice that the determined value of $\gamma(\omega)$ (Fig. 3) still has some instabilities at a few wavelengths. These are related to the way the coefficients are computed numerically [10], which is prone to resonances or instabilities. More precisely, the coefficients are obtained from the electric fields computed with the FMM and propagated to the far field, where the visibility of the interference pattern gives the magnitude and the location of the fringes gives the phase. Here any resonances or numerical instabilities instantly show in the magnitude of the coefficients, but the phase is mostly error free, as seen from Fig. 3. In this work we use only the complex value of the central frequency $\lambda_{\text{sp}} = 792\ \text{nm}$, which is free of the aforementioned instabilities.

TABLE II. Parameters used for all FMM calculations. Here D is the computational period, and o is the truncation order. Note that the period includes the two PML zones, which also contain the coordinate transform zones, as illustrated in Fig. 6(a).

Calculation	D (μm)	o
Figs. 2(a)–2(d)	100	1500
Figs. 2(e) and 4(a)	400	3500
Coefficients (Fig. 3)	170	2500

- [1] S. A. Maier, *Plasmonics: Fundamentals and Applications* (Springer, New York, NY, 2007).
- [2] W. L. Barnes, A. Dereux, and T. W. Ebbesen, Surface plasmon subwavelength optics, *Nature (London)* **424**, 824 (2003).
- [3] Z. Liu, J. M. Steele, H. Lee, and X. Zhang, Tuning the focus of a plasmonic lens, *Appl. Phys. Lett.* **88**, 171108 (2006).
- [4] P. Genevet, N. Yu, F. Aieta, J. Lin, M. A. Kats, R. Blanchard, M. O. Scully, Z. Gaburro, and F. Capasso, Ultra-thin plasmonic optical vortex plate based on phase discontinuities, *Appl. Phys. Lett.* **100**, 013101 (2012).
- [5] D. Xu, X. Xiong, L. Wu, X.-F. Ren, C. E. Png, G.-C. Guo, Q. Gong, and Y.-F. Xiao, Quantum plasmonics: New opportunity in fundamental and applied photonics, *Adv. Opt. Photonics* **10**, 703 (2018).
- [6] H. F. Schouten, N. Kuzmin, G. Dubois, T. D. Visser, G. Gbur, P. F. A. Alkemade, H. Blok, G. W. 't Hooft, D. Lenstra, and E. R. Eliel, Plasmon-Assisted Two-Slit Transmission: Young's Experiment Revisited, *Phys. Rev. Lett.* **94**, 053901 (2005).
- [7] C. H. Gan, G. Gbur, and T. D. Visser, Surface Plasmons Modulate the Spatial Coherence of Light in Young's Interference, *Phys. Rev. Lett.* **98**, 043908 (2007).
- [8] S. Divitt, M. Frimmer, T. D. Visser, and L. Novotny, Modulation of optical spatial coherence by surface plasmon polaritons, *Opt. Lett.* **41**, 3094 (2016).
- [9] Y. Chen, A. Norrman, S. A. Ponomarenko, and A. T. Friberg, Optical coherence and electromagnetic surface waves, *Prog. Opt.* **65**, 105 (2020).
- [10] A. Leinonen, K. Saastamoinen, H. Pesonen, G. Wu, T. D. Visser, J. Turunen, and A. T. Friberg, Polarization modulation by surface plasmons in Young's double-slit setup, *Phys. Rev. A* **104**, 043503 (2021).
- [11] X. Li, Q. Tan, B. Bai, and G. Jin, Experimental demonstration of tunable directional excitation of surface plasmon polaritons with a subwavelength metallic double slit, *Appl. Phys. Lett.* **98**, 251109 (2011).
- [12] Y. Sonnefraud, S. Kerman, G. Di Martino, D. Y. Lei, and S. A. Maier, Directional excitation of surface plasmon polaritons via nanoslits under varied incidence observed using leakage radiation microscopy, *Opt. Express* **20**, 4893 (2012).
- [13] S. B. Raghunathan, C. H. Gan, T. van Dijk, B. Ea Kim, H. F. Schouten, W. Ubachs, P. Lalanne, and T. D. Visser, Plasmon switching: Observation of dynamic surface plasmon steering by selective mode excitation in a sub-wavelength slit, *Opt. Express* **20**, 15326 (2012).
- [14] A. V. Zayats, I. I. Smolyaninov, A. A. Maradudin, Nano-optics of surface plasmon polaritons, *Phys. Rep.* **408**, 131 (2005).
- [15] K. G. Lee and Q. H. Park, Coupling of Surface Plasmon Polaritons and Light in Metallic Nanoslits, *Phys. Rev. Lett.* **95**, 103902 (2005).
- [16] P. Lalanne, J. P. Hugonin, and J. C. Rodler, Theory of Surface Plasmon Generation at Nanoslit Apertures, *Phys. Rev. Lett.* **95**, 263902 (2005).
- [17] F. van Beijnum, J. Sirre, C. Rétif, and M. P. van Exter, Speckle correlation functions applied to surface plasmons, *Phys. Rev. B* **85**, 035437 (2012).
- [18] R. C. Weast, *CRC Handbook of Chemistry and Physics*, 64th ed. (CRC Press, Boca Raton, FL, 1983).
- [19] H. Kim, J. Park, and B. Lee, *Fourier Modal Method and Its Applications in Computational Nanophotonics* (CRC Press, Boca Raton, FL, 2017).
- [20] N. Anttu, H. Mäntynen, A. Sorokina, J. Turunen, T. Sadi, and H. Lipsanen, Applied electromagnetic optics simulations for nanophotonics, *J. Appl. Phys.* **129**, 131102 (2021).
- [21] T. Vallius, P. Vahimaa, and J. Turunen, Pulse deformations at guided-mode resonance filters, *Opt. Express* **10**, 840 (2002).
- [22] See Supplemental Material at <http://link.aps.org/supplemental/10.1103/PhysRevA.106.063519> for a video of surface plasmon pulse propagation in the near field.
- [23] X. Yan and X. Su, *Linear Regression Analysis: Theory and Computing* (World Scientific, Singapore, 2009).
- [24] E. Wolf, Lecture 7.1: Analyticity, causality and dispersion relations, in *Selected Works of Emil Wolf with Commentary* (World Scientific, Singapore, 2001), p. 577.
- [25] L. Mandel and E. Wolf, *Optical Coherence and Quantum Optics* (Cambridge University Press, Cambridge, 1995).
- [26] Z. L. Sámson, P. Horak, K. F. MacDonald, and N. I. Zheludev, Femtosecond surface plasmon pulse propagation, *Opt. Lett.* **36**, 250 (2011).
- [27] S. Boscolo and C. Finot, Nonlinear pulse shaping in fibers for pulse generation and optical processing, *Int. J. Opt.* **2012**, 159057 (2012).
- [28] G. Gbur and T. D. Visser, Young's interference experiment: Past, present and future, *Prog. Opt.* **67**, 275 (2022).